Electromechanical Behavior of Interdigitated SiO_2 Cantilever Arrays

2010 Chinese Phys. Lett. 27 028503

(http://iopscience.iop.org/0256-307X/27/2/028503)

CHIN. PHYS. LETT. Vol. 27, No. 2 (2010) 028503

Electromechanical Behavior of Interdigitated SiO_2 Cantilever Arrays *

GUAN Zhi-Qiang(管志强)[1**], LUO Gang(罗刚)[2], MONTELIUS Lars[2], XU Hong-Xing(徐红星)[1,2]

[1]*Nanoscale Physics and Devices Laboratory, Institute of Physics, Chinese Academy of Sciences, Beijing 100190*

[2]*Division of Solid State Physics/The Nanometer Structure Consortium, Lund University, Lund S-221 00, Sweden*

(Received 16 November 2009)

Bending and first flexural mode vibration behavior of electrostatic actuated nanometer-sized interdigitated cantilever arrays are characterized under vacuum conditions. The "pull-in" effect in dc driving and the "hard spring effect" in ac driving are observed. A mass sensitivity of 20 fg is expected for our devices due to the ultra-small mass of the arm and relative high Q factor. The mass-spring lump model combined with Green's function method is used to fit the dc driving behaviors including the pull-in voltage. For the ac driving case, the polynomial expansion of the capacitive force is used in the model. The successfully fittings of the pull-in voltage and the hard spring effect prove that our simulation method could be used for guiding the geometrical design of cantilever-based sensors.

PACS: 85. 85. +j, 62. 25. −g, 62. 30. +d DOI: 10.1088/0256-307X/27/2/028503

Cantilever-based devices are one of the key elements of micro and nano electromechanical systems (MEMS and NEMS), with wide applications such as sensing[1−3] and energy harvesting.[4] Their unique combination of transducing properties, high quality factor and scalability to nanometer scale dimensions provide the cantilever-based sensors with high sensitivity and with a wide range of sensing domains. One of the most common sensing applications is mass sensors in which the adsorbed material will increase the mass of the cantilever, thereby causing a change in the resonant frequency which can be detected. It has been demonstrated that an improvement in sensitivity, power consumption and spatial resolution can be attained by reducing the cantilever dimensions to the nanometer range. Zeptogram mass resolution is reported for a single nanowire.[5,6] Integrating cantilever arrays is another research trend which could offer multiple sensing or increase the versatility of the mass sensor detection. Furthermore, the combination of the CBS with CMOS technology can integrate the electronic actuation and readout on the device and thereby reach extremely compact devices for gaseous detection.[7]

In this Letter, we investigate the deflection and first-order vibration behavior of an electrostatic actuated laterally movement interdigitated SiO_2 cantilever array under vacuum conditions. The deflection curve under dc voltage and the pull-in voltage are measured and fitted by the mass-spring lump model combined with Green's function method. The hard spring effect is observed in the ac driving case when the driving voltages exceed the critical value. The polynomial expansion of the capacitive force and a cubic term of the displacement are used in the model for demonstrating the ac driving behavior.

The cantilever arrays with interdigitated tuning fork structures and contact pads for electrical connection were fabricated on a one-inch wafer with an 850-nm-thick SiO_2 layer. The nano-fabrication processes involve thermal nanoimprint lithography (NIL), deep-UV lithography, ICP-reactive ion etching (ICP-RIE), and finally thermal evaporation of 5 nm Cr/40 nm Au. Details have been given elsewhere.[8] Scanning electron microscopy (SEM) is used to determine the cantilever geometrical parameters, i.e. length l, width w, thickness h, and gap distance s, as demonstrated in Fig. 1. The cantilever arms are hanging around 1.5 μm over the wafer substrate. The thickness of SiO_2 is 850 nm, thick enough to confine the movement in the lateral direction. The Cr/Au layer serves as an electrically actuate layer. Au also serves as a functional layer as a large selection of materials can be chemically absorbed by the thiol-group on gold, which is specially developed in biochip applications, such as DNA and protein detection. Measurements of mechanical properties are carried out *in-situ* in scanning electron microscope equipment (FEI FIB-SEM system FEI 200 apparatus, 10^{-5} Torr) at room temperature. The cantilever arrays are grounded to the chamber on one contact pad and applied voltage by an OMNI probe on another contact pad. A source measure unit (SMU) is used for a dc source while the ac voltage is generated sinusoidally by a Hewlett Packard 33120A waveform generator. The imaging system of the microscope is employed for displacement recording.

For the theoretical modeling, we consider the case of a slender beam experiencing moderate deflections and assume that shear deformations and Poisson effects are negligible. The cantilever vibration is in the small displacement condition ($s/L \approx 0.02$) for our measurements, thus the model is valid here. For the multilayer cantilever, we estimate the product of Young's modulus E and inertia moment I by $EI =$

*Supported by the National Basic Research Program of China under Grant Nos 2006DFB02020 and 2007CB936800, and the One-Hundred Persons Project of Chinese Academy of Sciences.

**Email: guzhqi@aphy.iphy.ac.cn

$w^3 \sum h_i E_i/12$. Young's modulus and densities of Au, Cr and SiO_2 are taken from published data.[9] The total mass of SiO_2, Cr and Au is estimated to be $m_0 = 9.9\,\text{pg}$.

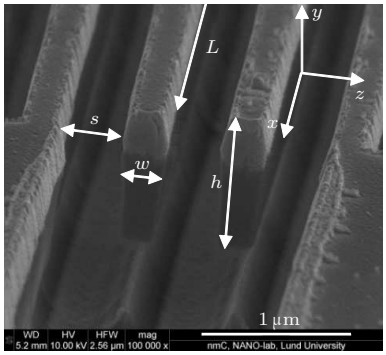

Fig. 1. Tilted SEM image of the interdigitated cantilever structure. The light colored part on top is the Au coating layer. Geometrical parameters are $l = 15\,\mu\text{m}$, $w = 250\,\text{nm}$, $s = 230$–$450\,\text{nm}$.

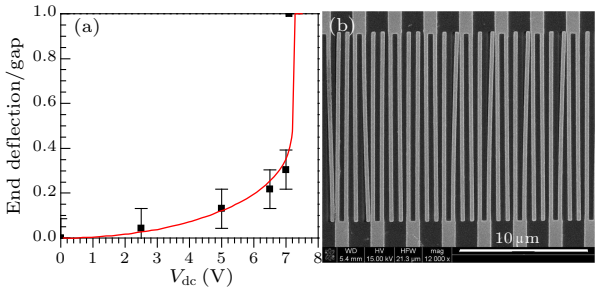

Fig. 2. (a) Normalized cantilever end deflection vs applied dc voltage measured on one arm. Black squares with error bars are measured data. The red curve is the modeling result. (b) SEM image of pull-in phenomenon at $V_{dc} = 7.1\,\text{V}$.

The bending measurements were carried out by applying dc voltage and measuring the cantilever end displacements on one chosen arm. The dc voltage increased from 0 V to 7.1 V until the pull-in effect was observed, which happened when the mechanical restoring force of the beam could no longer resist the opposing electrostatic force and led to the collapse of the structure, see Fig. 2(b). The free end displacement versus the applied dc voltage is plotted in Fig. 2(a) by squares with error bars. The gap is $s = 230\,\text{nm}$. The pull-in voltage was measured to be 7.1 V, while the maximum end deflection was $Z(L) = 70 \pm 20\,\text{nm}$ and the maximum normalized end deflection $Z(L)/s \approx 0.33 \pm 0.08$, which is consistent with the published threshold data.[10] Notice that the pull-in effect is only observed for some arms because the gap values for SiO_2 arms are different due to different intrinsic stresses. Thus the pull-in behavior first happened for arms with smaller gaps and then the circuit was shortcut and the other arms recovered to the origin state.

For the dc driving modeling, the lateral cantilever movement is sliced to calculate the external force applied to the cantilever along its length. We introduce the dimensionless expression $z(x) = u(\hat{x})\hat{Z}s$, $\hat{x} = x/L$, where $u(\hat{x})$ is the curve function, $\hat{Z}$ is the end deflection normalized by s. The equation for each slide is

$$\frac{EIs}{L^4}\frac{d^4(\hat{Z}u)}{d\hat{x}^4} = \frac{\varepsilon_0 h' V_{\text{dc}}^2}{2s^2}\frac{1}{(1-\hat{Z}u)^2}. \tag{1}$$

The capacitive force is modified by effective area $h'L$, which is related to the effective gold surface area and is the only fitted parameter in our model. The axial load and mid-plane stretching are ignored in our simplified model. Using Green's function for the cantilever structures,[11]

$$G(x,\xi) = \begin{cases} \frac{x^2}{6}(3\xi - x), & 0 \le x < \xi, \\ \frac{\xi^2}{6}(3x - \xi), & \xi \le x < 1, \end{cases}$$

the solution to Eq. (1) becomes

$$\hat{Z}u(\hat{x}) = \frac{\varepsilon_0 h' V_{\text{dc}}^2 L^4}{2s^3 EI}\int_0^1 G(\hat{x},\hat{x}')\frac{1}{(1-\hat{Z}u(\hat{x}'))^2}d\hat{x}'. \tag{2}$$

Equation (2) is solved iteratively to obtain $\hat{Z}u(\hat{x})$. The fitting result is plotted in Fig. 2(a) (red curve). The fitted parameter $h' = 270\,\text{nm}$ is chosen to fit the pull-in voltage and serves to account, in part, for the crude approximation employed in the model. The experimental data and simulation curve fit quite well. Compared with Ref. [10], our device has $\alpha_1 \approx 5$, $\alpha_2 V_p^2 \approx 8$, thus the axial load is estimated to be $N \approx 10 \pm 2$, and the maximum normalized end deflection by our model is consistent with the multi mode analysis in Ref. [10]. Thus we could use the fitting parameter to predict pull-in voltages and avoid the malfunction of cantilever devices.

For the ac voltage driving case we will introduce the modeling first. The lateral cantilever movement is approximated by a spring-mass lumped model:

$$\rho h w\frac{\partial^2 z}{\partial t^2} + \mu\frac{\partial z}{\partial t} + EI\frac{\partial^4 z}{\partial x^4} = \frac{\varepsilon_0 h' V^2}{2(s-z)^2}. \tag{3}$$

Take the dimensionless expression $z(x,t) = s\hat{Z}(t)u(\hat{x})$ and use the curve function of the first order flexural mode of free resonance as an approximation: $u_1(\hat{x}) = 0.5[\cosh(\lambda\hat{x}) - \cos(\lambda\hat{x})] + 0.367[\sin(\lambda\hat{x}) - \sinh(\lambda\hat{x})]$. Integrate the equation along the arm length, the time-dependent set of equations related to each cantilever slide is simplified to a one-variable time-dependent problem:

$$M\ddot{\hat{Z}} + \mu_T\dot{\hat{Z}} + K_1\hat{Z} + K_3\hat{Z}^3 = F_{\text{cap}}/s, \tag{4}$$

where $M = 0.39m_0 = 0.39\rho hwL$, $K_1 = 0.39EI(1.8751)^4/L^3$, $\mu_T = 0.39\mu L = \frac{0.39}{Q}\left(\frac{1.8751}{L}\right)^2\sqrt{EIm_0}L$.

The term $K_3\hat{Z}^3$ is added to fit the nonlinear behavior in large bias voltage. Capacitive force is calculated

by

$$F_{\rm cap} = \frac{\varepsilon_0 h' L V_0^2 (1+\cos(2\Omega t))}{4s^2} \int_0^1 \frac{1}{(1-\hat{Z}u_1)^2} d\hat{x}$$
$$= F_0(t) \int_0^1 \frac{1}{(1-\hat{Z}u_1)^2} d\hat{x},$$

where $V = V_0 \cos(\Omega t)$ is the ac voltage, $h'L$ is the effective area which considers the effective counter surface, ε_0 is the dielectric constant of the vacuum. We use the polynomial fitting expression of capacitive force $F_{\rm cap} = F_0(t)[1 + a\hat{Z} + b\hat{Z}^2 + c\hat{Z}^3]$ with a, b, c fitted by comparison with integration results of u_1. The values of a, b, c are listed in Table 1. Taking $\hat{Z}(t) \approx a_1 \cos(\Omega_a t)$ in Eq. (4) and using the first-mode free resonant frequency $\Omega_0 = \sqrt{K_1/M}$, forced resonant frequency Ω_a, $\gamma = 3K_3/(8M\Omega_0)$ and $\lambda = \mu_T/2M$, approximation $\Omega_a = \Omega_0 + \omega \approx \Omega_0$, $\Omega_a^2 \approx \Omega_0^2 + 2\Omega_0\omega$, ignoring the constant term and higher frequency terms and only considering $\Omega_a t$ terms, we have

$$2a_1 M\Omega_0[-\omega\cos(\Omega_a t) + \gamma a_1^2 \cos(\Omega_a t) - \lambda \sin(\Omega_a t)]$$
$$\approx \frac{\varepsilon_0 h' L V_0^2}{4s^3}\left(1 + aa_1 + \frac{3b}{4}a_1^2 + \frac{3c}{4}a_1^3\right)\cos(\Omega_a t). \quad (5)$$

Introducing $f = \varepsilon_0 h' L V_0^2/(8s^3 M\Omega_0)$, $\sigma = (\omega^2 + \lambda^2)/f^2$, $D_1 = \gamma^2/f^2$, $D_2 = 2\omega\gamma/f^2$, because the moduli of both sides are equal to each other, we have

$$1 + 2aa_1 + \left(a^2 + \frac{3}{2}b - \sigma\right)a_1^2 + \frac{3}{2}(ab + c)a_1^3$$
$$+ \left(\left(\frac{3}{4}b\right)^2 + \frac{3}{2}ac + D_2\right)a_1^4 + \frac{9}{8}bca_1^5$$
$$+ \left(\left(\frac{3}{4}c\right)^2 - D_1\right)a_1^6 = 0. \quad (6)$$

Solving Eq. (6) we can obtain a_1 and thus the first flexural mode vibration amplitude $a_1 s$. A more strict analysis which takes $\hat{Z}(t) \approx a_0 + a_1 \cos(\Omega_a t)$ confirms $a_0 \ll a_1$, thus the $\hat{Z}(t) \approx a_1 \cos(\Omega_a t)$ approximation is reasonable.

Table 1. Polynomial expansion coefficients of capacitive force.

a	b	c	
1.12	1.67	1.02	$Z \in [-0.9, -0.5]$
0.77	0.93	1.03	$Z \in [-0.5, 0.5]$
2.46	−6.79	9.83	$Z \in [0.5, 0.7]$
12.38	−37.28	33.20	$Z \in [0.7, 0.8]$
72.53	−198.15	138.71	$Z \in [0.8, 0.9]$

With applied peak-to-peak voltage $V_{\rm PP} = 0.5$ V and driving frequency sweep from 400 kHz to 550 kHz in 60 s, the first flexural mode vibration of arms was recorded into a movie with two frames per second. The number of vibrating arms vs resonant frequency (the resonant frequency is doubled of the driving frequency) is plotted in Fig. 3. The first-mode resonant frequency 884 kHz derived by $f_1 = (1/2\pi)(1.8751/L)^2\sqrt{EIL/m_0}$ fits well with the measured value. The Q factor of a single arm is defined as $Q = f_1/\Delta f$ where Δf is the FWHM of the resonance peak in the frequency domain and is estimated within the range from 220 to 900. This value agrees with Sandberg's result in Ref. [12] in which the gold coating effect on reduction of the Q factor of the SiO_2 cantilever was studied and a Q factor of 400 was measured for the first flexural mode of a 100 nm gold coating SiO_2 cantilever in vacuum (50 Pa). The broad distribution of resonant frequency shows the susceptibility to the detailed geometry and intrinsic interlayer stress discrepancy. According to $\Delta m = 2m_0\Delta f/f_0$,[1] although the Q factor is only 900 for our device, the mass sensitivity (~ 20 fg) is still higher than the value published.[13] It is also suggested to use a higher order vibration mode for higher sensitivity.[12]

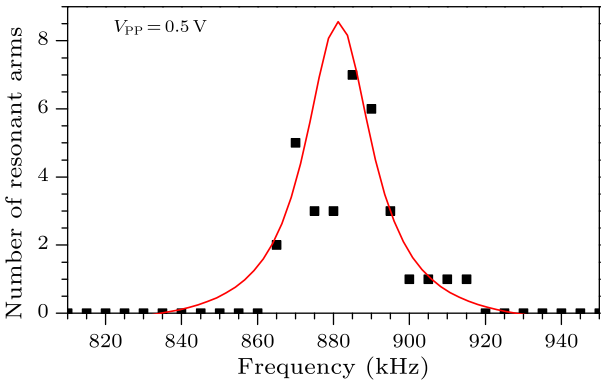

Fig. 3. Number of resonant vibration arms vs resonant frequency, $V_{\rm PP} = 0.5$ V. Black squares are the measurement data. The red curve is the Lorentz fitting result.

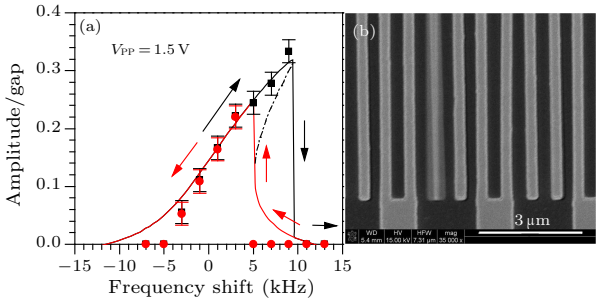

Fig. 4. (a) Normalized amplitude vs resonant frequency shift. The symbols are the measured data. Curves are the simulation results. Black and red colors indicate the sweep direction: black upwards, red downwards. The black dashed line is the metastable eigenvalue of Eq. (6). The hard spring effect is observed. The resonant frequency origin corresponds to 884 kHz. $V_{\rm PP} = 1.5$ V. (b) SEM image of a single vibrating arm.

The normalized amplitude vs resonant frequency shift was measured for one arm, illustrated in Fig. 4(a) for $V_{\rm PP} = 1.5$ V, $s = 360$ nm, $Q = 270$. Nonlinear behavior, or more precisely, the hard spring effect[14–16] is observed. When the driving frequency sweeps upwards around the resonant frequency f_0, the vibration amplitude will increase first and then jump down at a frequency f_1 larger than f_0; when the driving frequency sweeps downwards, the amplitude will jump

up to a lower value at a frequency between f_0 and f_1, then decrease gradually.[17] Similar nonlinear behavior has been studied in Refs. [18–21] and explained by the cubic nonlinearity of the restoring force. Thus the cubic term is introduced in Eq. (4) and is likely due to the mid-plane stretching effect. The solution of the equation shows that at a high driving voltage, Eq. (6) has triple eigenvalues in a certain range of frequency and two values are stable [see Fig. 4(a)], thus resulting in discontinuities in the measured response curve. Fitting parameters are $h' = 630\,\text{nm}$ and $K_3 = 0.066$ in our model. Here h' is larger than the dc simulation value because of extra loss of ac driving. The positive K_3 indicates that the hard spring effect happened in our case.[20]

The normalized amplitude and resonant frequency shift vs the applied ac voltage (V_{PP} is from 1.5 V to 2.2 V) are measured and fitted by the model [see Figs. 5(a) and 5(b)]. The normalized amplitude could reach a higher value (~ 0.6) compared with the dc driving (~ 0.3). The slope of the frequency curve vs voltage becomes larger when the driving voltage exceeds the critical values, which indicates that higher frequency sensitivity is possible in the nonlinear region. The amplitude "jump" phenomenon can also be utilized to realize ultra-high sensitivity sensors or switches.[20] Our simulation gives the critical voltage of $V_{\text{PP}} = 1\,\text{V}$ [Fig. 5(c)]. The good fitting and onset voltage prediction of the hard spring effect allow us to optimize the device design and finally achieve an ultra-high sensing device by utilizing the nonlinear behavior of cantilever structures.

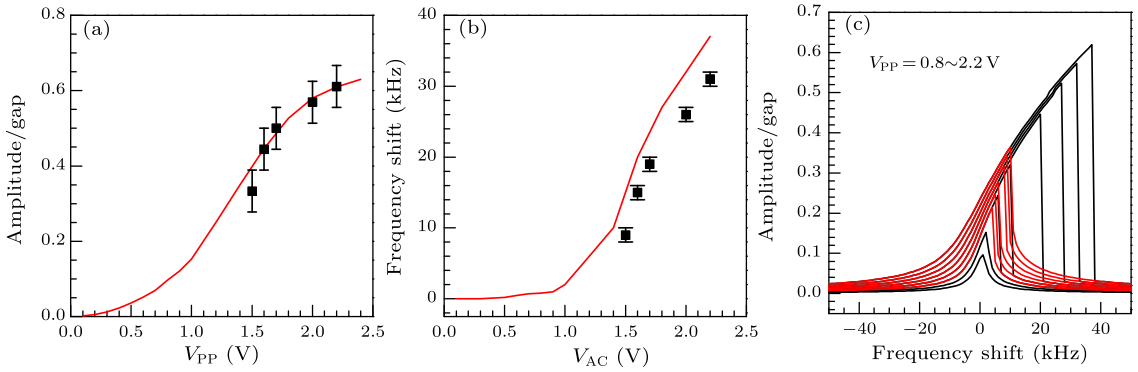

Fig. 5. (a) Normalized amplitude vs applied ac voltage, (b) resonant frequency shift vs applied ac voltage. Black symbols with error bars are the measured data. Red curves are the simulation results. $V_{\text{PP}} = 1.5$–$2.2\,\text{V}$. (c) Simulation of curves for normalized amplitude vs resonant frequency shift. $V_{\text{PP}} = 0.8$–$2.2\,\text{V}$.

In summary, we have characterized the static and dynamic behavior of the interdigitated SiO_2 cantilever arrays under vacuum conditions. The pull-in effect and a maximum normalized reflection of 0.33 are observed under dc driving. For ac driving the hard spring effect appears when the driving voltage exceeds the critical value. The measurements of first flexural mode resonant frequency and Q factors indicate that the high mass sensitivity of a femtogram could be attained by our nanometer-sized cantilever arrays. The mass-spring lump model combined with Green's function method is introduced to fit the dc-driving deflection curve, including the fitting of the pull-in voltage. For the ac driving case, the polynomial expansion of capacitive force and an additional cubic term of the displacement are used in the equations to simulate the hard spring effect and to fit the onset voltage of the nonlinear behavior. The good agreement between experiments and simulations encourages us to use the simulation to help the design of the cantilever structures in, for example, avoiding the malfunction of devices and utilizing the nonlinear behavior for ultra-high sensitivity sensing. With a deeper understanding of electromechanical behaviors of the interdigitated cantilever arrays, a multiple sensing and high sensitivity sensor could be developed and a variety of novel potential applications such as optical filters, switches could be expected.

We thank Hongqi Xu, Jiarui Yang and Ulf Hakanson for helpful discussion.

References

[1] Ziegler C 2004 *Anal. Bioanal. Chem.* **379** 946
[2] Thundat T et al 1997 *Microscale Therm. Eng.* **1** 185
[3] Yu X, Zhang D et al 2003 *Chin. Phys. Lett.* **20** 1637
[4] Fang H, Liu J, Xu Z et al 2006 *Chin. Phys. Lett.* **23** 732
[5] Nishio M et al 2005 *Appl. Phys. Lett.* **86** 133111
[6] Yang Y T et al 2006 *Nano Lett.* **6** 583
[7] Villarroya M et al 2006 *Sensors Actuators A* **132** 154
[8] Luo G, Maximov I et al 2006 *Nanotechnology* **17** 1906
[9] Sandberg R et al 2005 *J. Micromech. Microeng.* **15** 1454
[10] Zhang Y and Zhao Y 2006 *Sensors Actuators A* **127** 366
[11] Ramezani A et al 2007 *Int. J. Solids Struct.* **44** 4925
[12] Sandberg R et al 2005 *J. Micromech. Microeng.* **15** 2249
[13] Teva J, Abadal G et al 2006 *Ultramicroscopy* **106** 808
[14] Nicu L et al 2004 *J. Micromech. Microeng.* **14** 727
[15] Tilmans H A et al 1992 *Sensors Actuators A* **30** 35
[16] Gui C Q et al 1998 *J. Microelectromech. Suppl.* **7** 122
[17] Nayfeh A H and Mook D T 1995 *Nonlinear Oscillations* (New York: Wiley) p 163
[18] Husain A, Hone J, Postma H W et al 2003 *Appl. Phys. Lett.* **83** 1240
[19] Requa M V, Turner K L 2006 *Appl. Phys. Lett.* **88** 263508
[20] Keskar G et al 2008 *IEEE Sensors J.* **8** 1848
[21] Zhang J and O S S 2003 *Sensors Actuators B* **94** 65